Upgrading of g-C_3N_4 semiconductor by a Nitrogen-doped carbon material: A photocatalytic degradation application.

Nijad Ishak[1*], Velu Jeyalakshmi[1], Milena Setka[1], Mathieu Grandcolas[2], Balamurugan Devadas[3] and Miroslav Šoóš[1*]

[1] University of Chemistry and Technology Prague, Department of Chemical Engineering, Technická 3, Prague, Czech Republic

[2] SINTEF Industry, Department of Sustainable Energy Technology, 0373 Oslo, Norway

[3] University of Chemistry and Technology Prague, Department of Inorganic Technology, Technická 5, Prague, Czech Republic

*Corresponding author: ishakj@vscht.cz, miroslav.soos@vscht.cz

Abstract

The synthesis of a cheap, nonmetallic and active photocatalyst is the target of this study. Several Carbon loadings (0.2, 0.5 and 1 wt.%) were incorporated into the graphitic carbon nitride (g-C_3N_4) semiconductor by a simple wet impregnation method. Temperature treatment was used for composite photocatalyst activation. The catalysts and their precursors were characterized by N_2 sorption, X-ray diffraction (XRD), transmission electron microscopy (TEM), Fourier Transform Infrared Spectroscopy (FTIR), X-ray photoelectron spectroscopy (XPS), thermal gravimetric analysis (TGA), ultraviolet-visible spectroscopy (UV-vis) and Raman spectroscopy. The sample composed of 0.5 wt.% N-Carbon/g-C_3N_4 treated 2 hours at 500°C revealed the best performance by showing the highest degradation efficiency of methylene blue (MB) (90% in 3 hours using solar light simulator). The optimal amount of catalyst in the medium was determined to be 1g/L. The high activity of the treated 0.5 wt.% N-Carbon/g-C_3N_4 catalyst was ascribed to an improvement in the electrochemical properties of the bulk g-C_3N_4 as a result of the inclusion of nitrogen-doped carbon in its core structure. The intensification of conductivity and the improvement in the electrochemical properties was explained by the formation of carbon-like graphitic structure doped with pyridinic and pyrrolic nitrogen groups under heat treatment. The high

activity, stability, low cost and non-toxicity of this material prove the high potential of this technology for water purification and other related fields.

Keywords

Photocatalysis, degradation, methylene blue, Carbon nitrides, Nitrogen-doped Carbon.

1. Introduction

Over the last few years, there has been a surge in interest in photocatalysis [1]. Due to its particular redox function and its dependence on sunlight as a renewable energy source, it is highly successful and recommended in the remediation of environmental contaminants and in the breakdown of organic molecules [2]. Photocatalysts made of semiconductor particles are appropriate for this process [3]. Due to its outstanding photochemical stability, non-toxicity, and strong photocatalytic potential, TiO_2 is the most intensively studied semiconductor. However, TiO_2 can only drive photocatalysis when excited by UV light, which accounts for approximately only 4% of sunlight, severely limiting its practical applicability [4]. Furthermore, the potential of harmful metals leaching during the photocatalytic process is a key problem with these semiconductor composites. Nontoxicity and insolubility, both in the dark and in the light, are important concerns in water treatment techniques employing semiconductors.

Carbon nitride (C_3N_4), has recently sparked interest as a potential photocatalyst due to its unique properties, including a unique electronic and optical structure, as well as high chemical and thermal stability. Due to their advantageous solar absorption, and exposed reactive sites, various innovative nanostructured C_3N_4-based photocatalysts, including 1D nanorods [5], 2D nanosheets [6], and 3D hierarchical structures [7], have been intensively developed in recent years. On the other hand, the photocatalytic effectiveness of bare g-C_3N_4 was far from ideal due to the few active sites present [8]. To improve the photocatalytic activity of g-C_3N_4, many approaches have been used, including creating a suitable textural porosity [9], doping with metal or non-metal elements [10], and exfoliation of the bulk phase to nanosheets [11]. The easiest and most effective method for creating heterojunctions with g-

C_3N_4 is believed to be noble metal and heteroatom doping. However, noble metals are expensive and have a limited supply [12].

Carbon material is commonly used in catalysis due to its physical and chemical characteristics, nontoxicity, and conductivity that enhance electron-hole separation [13]. Heterogeneous doping of carbon with nitrogen (N-Carbon) has been shown to increase photocatalytic performance because it promotes the charge delocalization and carbon surface modification [14]. According to a research by Li et al., carbon material can act as electron reservoirs, trapping photoexcited electrons and resulting in improved charge separation efficiency [15]. Moreover, two π-conjugated systems (g-C_3N_4 and carbon) can stabilize the hybrids and produce photocatalytic synergy [16]. In light of this, extending and delocalizing the aromatic π-conjugated system by combining carbonaceous materials with g-C_3N_4 is anticipated to improve the photocatalytic performance by improving the separation and transfer of charge carriers [17]. As a result, the composite development of N-Carbon/g-C_3N_4 serves a crucial function, namely the enhancement of photodegradation performance by improvement electron transfer. Although the hybridization of N-Carbon and g-C_3N_4 already exists in the literature [18, 19] the reason behind the application of a heat treatment on the hybrid material is not reported and its effect on the chemical structure of the material is not clearly explained. In fact, many authors reported the application of heat treatment on the composite formed by g-C_3N_4 and carbon either by hydrothermal method [20] or by heat polymerization [21]. However, to our knowledge, a description on the effect of heat treatment on the structural properties of the composite formed by g-C_3N_4 and carbon is not present in the literature. Therefore, the target of this study is to disclose the reason behind the application of heat treatment by characterizing the material before and after heat treatment and by testing its photocatalytic activity. The studied material was synthesized by mixing the microwave produced carbon material and g-C_3N_4 followed by drying. For catalytic activity test, degradation of MB was chosen as an application. The chosen precursors for the carbon material were citric acid and urea, while g-C_3N_4 precursor was melamine. These precursors are inexpensive and widely accessible materials. In addition, the carbon material was produced by the low-cost and fast microwave method, which requires significantly less energy and time of synthesis than the hydrothermal method and it is giving a higher yield of product while conserving the properties [22]. Therefore, in this study, the best amount of carbon doping was

investigated, the structural changes on the hybrid composite formed by carbon and g-C_3N_4 after heat treatment were explored, and hence, the reasons of applying heat treatment was finally divulged. This finding actually paves the way for further investigation into carbon doped semiconductors. In fact, the ability of charge alteration through carbon doping could provide a booming in the architecture of material having a specific required conductivity and a determined charge flow direction. These materials could be employed in the domain of electronics, thin-film transistors and photovoltaics [23, 24].

2. Material and Methods

2.1. Materials

Citric acid monohydrate (> 99.9 %), Urea (> 99.5 %), Melamine (> 99 %) and MB; were all purchased from Sigma Aldrich. Ultra-pure water was used throughout all experiments.

2.2. Synthesis of Carbon by the microwave method:

1 g of urea and 3 g of citric acid (1/1 molar ratio) are dissolved with 10 mL of deionized water in a 50 mL beaker and mixed for 30 min until the solution becomes transparent. The mixture was then placed in a household microwave oven and treated for 10 min and 750 W. The black material obtained (Figure S1) is then mixed with 50 mL of deionized water for 30 min and sonicated for 1 hour. In order to purify the mixture and remove agglomerated particles, the mixture is centrifuged at 10 000 rpm for 30 min. The samples are then placed in the dark.

2.3. Synthesis of g-C_3N_4:

Melamine precursor is used to synthesize the g-C_3N_4 semiconductor (Figure S3). Melamine was adopted as a precursor for g-C_3N_4 synthesis instead of urea since it is giving a higher weight yield (Figure S4). 20 g of melamine were treated at temperature of 450, 500 or 550°C for 3 hours in air environment (heating ramp of 1, 2 or 10°C/min) in order to optimize synthesis methodology based on chemical structure and weight yield. When the oven cools to ambient temperature, the covered crucible is removed, and a yellowish powder is collected and grinded. This sample is noted g-C_3N_4.

2.4. Synthesis of Carbon/g-C_3N_4 and N-Carbon/g-C_3N_4

Carbon/g-C_3N_4 samples were prepared using the wet impregnation method. The required weight of Carbon was added to 1 g of g-C_3N_4 in order to produce 0.2, 0.5 and 1 wt.% Carbon/g-C_3N_4. After mixing

overnight with 20 mL deionized water, the solutions were sonicated for 3 hours in a sonication bath and dried overnight at 80°C. Half of each obtained sample was subjected to a heat treatment in an air environment at 500°C in a closed crucible, the nitrogen is anticipated to become doped, hence, samples are named treated 0.2N-Carbon/g-C_3N_4, treated 0.5N-Carbon/g-C_3N_4 and treated 1N-Carbon/g-C_3N_4. The scheme of X%N-Carbon/g-C_3N_4 synthesis is shown in Figure 1.

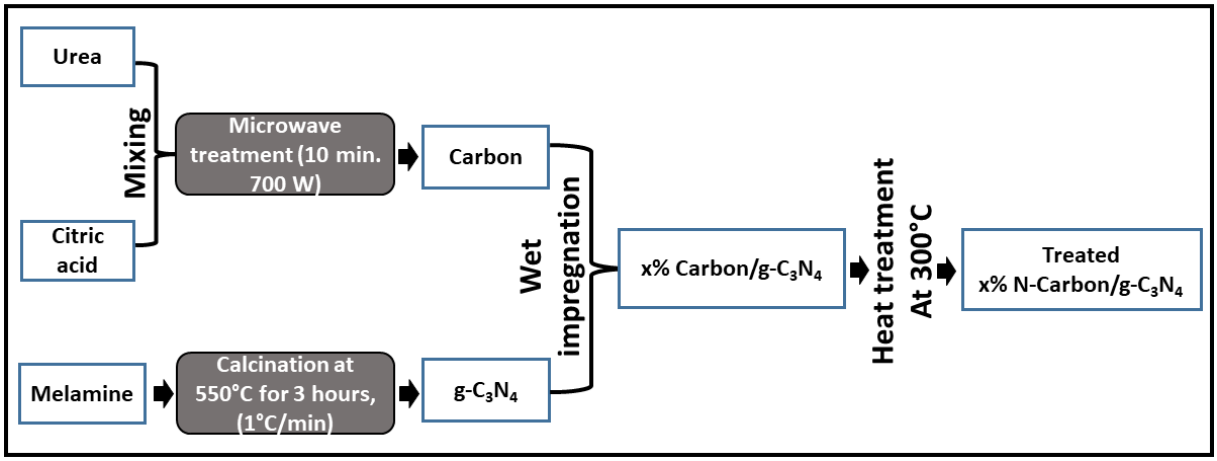

Figure 1: X%N-Carbon/g-C_3N_4 synthesis schematic.

2.5. Material Characterization

An EFTEM Jeol 2200 FS microscope was used to perform high-resolution transmission electron microscopy (HR-TEM). The acceleration voltage utilized for measurement was 200 keV. The TEM sample was dispersed in water (1 mg. mL^{-1} in water), dropped cast on a TEM grid (Cu; 200 mesh; Formvar/carbon) and dried at 60°C for 12 hours. X-ray diffractograms were recorded on a PANanalytical X'Pert^3 Powder using *CuK*α radiation (λ = 1.5418 Å, U = 40 kV, I = 30 mA) over a 2θ range of 5 to 50° with a step size of 0.04°. The FTIR spectra of the samples were measured in KBr pellets using a Nicolet 6700 FTIR spectrometer under the specified conditions using 64 scans covering the wavelength range 400–4000 cm^{-1}, with a resolution of 2 cm^{-1}. Raman spectra were measured on a Thermo Scientific DXR Raman Microscope equipped with a diode laser of excitation of 532 nm, 633 nm, 780 nm and 1064 nm. PL was measured using the Shamrock 300i spectrograph (Andor, Oxford Instruments) with an EMCCD camera (Newton 971, Andor, Oxford Instruments). At 325 nm, a standard He-Cd laser system was used to generate the excitation. The surface chemistry of the samples was analyzed with X-ray photoelectron spectroscopy (Kratos Axis Supra, Manchester, UK) with

monochromatic Al Kα X-ray radiation. A pass energy of 80 eV and 20 eV, respectively, was used to measure the wide and narrow spectra. Based on the C-C peak at a binding energy of 284.8 eV, XPS spectra were calibrated. The specific surface area of the prepared materials were characterized by Quantachrome NOVA 2200e and Micrometrics 3Flex Adsorption Analysers. Thermogravimetric Analysis (TGA) studies were performed on a Setaram Labsys EVO device. 10 mg of catalyst was deposited in an alumina crucible that was inserted into the system. The sample was heated from ambient temperature to 800°C (heating ramp 5 °C/min) using an air flow (50 mL/min). The band gap of the prepared catalysts was measured using an Agilent Cary 60 UV-vis equipped with a Diffuse Reflectance Accessory. In order to plot the Tauc plot, Eq.1. was adopted [25]:

$$(F(R)hv)^2 = \left(\frac{1240\,(1-R^2)}{2R\lambda}\right)^2 \quad (1)$$

Where R is the reflectance at the corresponding wavelength $\boldsymbol{\lambda}$.

Data collection and processing were performed using Thermo Scientific OMNIC 8.0 software (ThermoFisher Scientific, Waltham, MA, USA). The data were plotted and analyzed using the Origin 2019b Pro software package.

2.6. Photoelectrochemical measurements

A conventional three-electrode arrangement was used to determine the conductivity and resistance of the studied materials. Linear sweep voltammetry (LSV) was performed at a scan rate of 5 mV/s in an electrolyte solution of 0.5 M H_2SO_4. The counter and reference electrodes were Pt and Ag/AgCl in a 3.5 M KCl solution, respectively. These procedures were used to create the working electrodes: Under ultrasonication, 6 mg of the freshly synthesized sample was mixed with 60 μL of a 5 wt.% Nafion solution. Then, after drying at room temperature, the obtained powder was applied to the polished glassy carbon electrode. Electrochemical impedance spectroscopy (EIS) was performed at − 0.2V bias potential.

2.7. Photocatalytic test and kinetic study

Photocatalytic testing was performed in a 100 mL quartz container using MB (10 mg/L) as a model compound (Figure S10). The photocatalyst was first dispersed at a concentration of 1 g/L and mechanically stirred in MB solution in complete darkness for a minimum of 2 h to ensure complete

adsorption equilibrium. The suspension was then horizontally irradiated with a 300 W solar simulator (Asahi Spectra, model HAL-320) at a distance so that 1 SUN (100 mW/cm^2) could be detected with a calibrated reference Si PV cell (Newport, model 91150 V). At interval times, 2 mL samples are taken, filtered at 0.2 µm and analysed by UV-vis spectrophotometry (Agilent CARY 5000). To conduct the cyclic study, the catalyst was separated by filtration at the end of the degradation experiment, washed many times with ethanol to remove the adsorbed MB and then dried at 80°C. The absorption value at 665 nm was used to follow the kinetics of degradation. The catalytic activity of the materials in question was studied by means of the reaction kinetics.

The degradation efficiency of the studied materials was calculated by Eq.2.

$$\text{Degradation efficiency (\%)} = \frac{C_0 - C}{C_0} \times 100, \quad (2)$$

Where C_0 is the concentration of MB in the solution at the end of the adsorption phase, and C is the concentration of MB after being exposed to light irradiation.

3. Results and discussion

3.1. Optimization of g-C_3N_4 production

The weight yield (wt.%) of g-C_3N_4 synthetized from melamine precursor was investigated with the change of temperature and ramp of calcination and the results are shown in Figure 2a. The temperatures of calcination ranged from 450 to 550°C and the ramps chosen were 1, 5 and 10°C/min. The weight yield of g-C_3N_4 was highest at a lower temperature of calcination and at a lower ramp, while it is the lowest when the temperature is the highest at 550°C with a ramp of 10°C/min. Figure S5 in supporting information part shows an increase in the intensity of the yellowish color when the melamine is treated at 550°C and the FTIR spectra in Figure 2b shows more peaks in the region of C-N heterocycles for this sample. The XRD patterns in Figure S6 shows the characteristic peak of g-C_3N_4 at $2\theta = 27.62°$ for the sample calcined at 550°C, whereas at other temperatures, other peaks are appearing and shifts are detected. Therefore, it can be inferred from all these observations that the complete polymerization of g-C_3N_4 occurs at the highest temperature of 550°C. The reaction ramp of 1°C/min was adopted since it gave the highest yield. Hence, these conditions were adopted in our studies.

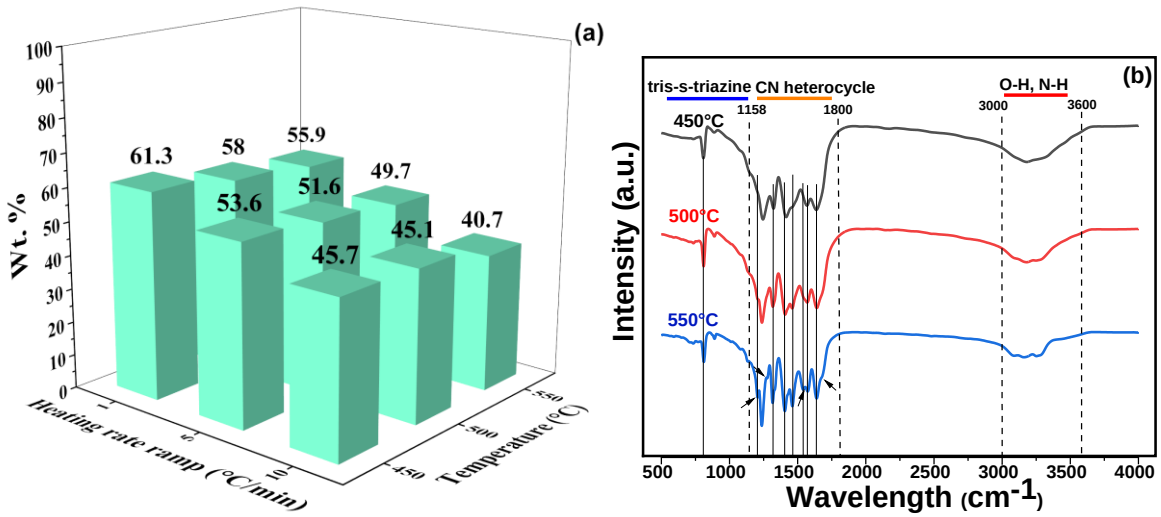

Figure 2: (a)Influence of temperature and ramp of treatment on g-C_3N_4 yield, (b)FTIR spectra of g-C_3N_4 samples prepared at different temperatures.

3.2. Catalyst characterization

3.2.1. Characterization of g-C_3N_4 , Carbon/g-C_3N_4 and treated N-Carbon/g-C_3N_4

X-Ray diffraction (XRD) patterns (Figure 3a) show the same characteristic peak at 27.62° for g-C_3N_4 and 0.5Carbon/g-C_3N_4 corresponding to the 002 plane in all the samples [26, 27]. Thermally treated 0.5N-Carbon doped on g-C_3N_4 (Treated 0.5N-Carbon/g-C_3N_4) maintained the crystallinity while a tiny shift in phase is seen towards the right of the characteristic peak (2θ = 27.73°). It can be inferred from this result that the thermal treatment of 0.5N-Carbon/g-C_3N_4 led to a change in the interlayer aromatic packing of the 0.5N-Carbon/g-C_3N_4 toward a denser layer packing [28]. The shift was attributed to an increase in the interaction between layers resulting in the interlayer distance reduction [29]. A closer image to the peak is present in the supporting information part (Figure S9). When it comes to carbon, the intense peak centered at 2θ = 27° corresponds to the (002) planes of graphite [30]. However, this peak faded when the sample was exposed to a heat treatment at 500°C and the sample became completely amorphous. These findings revealed that the structure of the condensed graphitic carbon nitride was significantly altered by the insertion of N-Carbon material.

The chemical structure of the pristine g-C_3N_4 and Carbon/g-C_3N_4 and treated N-Carbon/g-C_3N_4 was determined by FTIR measurements and the results are shown in Figure 3b. The three samples under

investigation presented the same FTIR spectra. The three samples showed the broad band between 3000 and 3500 cm^{-1} that is assigned to N – H and O – H groups [31]. A group of intense bands is detected between 1200 cm^{-1} and 1650 cm^{-1}. The band at 1640 cm^{-1} is assigned to C – N stretching, although the bands at 1555 cm^{-1}, 1461 cm^{-1} and 1405 cm^{-1} correspond to the C – N heterocycles in stretching vibration modes [32-34]. The bands at 1319 cm^{-1} and 1243 cm^{-1} are assigned to the vibration of C – NH – C connected units [35]. Moreover, the typical tri-s-triazine rings are detected by the strong peak seen at 810 cm^{-1} [36]. The FTIR spectra of Carbon show absorption bands between 3500 cm^{-1} and 2800 cm^{-1}, which are attributed to the stretching vibrations of O – H, N – H and C H. The particular band at 1720 cm^{-1} is assigned to the stretching of the carboxylic groups C = O. Furthermore, the bending vibration of C–H and the stretching vibration of the acyl group R – C = O are responsible for the two significant absorption bands at 1404 cm^{-1} and 1220 cm^{-1}, respectively [37]. The similarity of FTIR profile of Carbon/g-C_3N_4 and g-C_3N_4 sample could be explained by the low amount of carbon material (0.5 wt.%) impregnated on the g-C_3N_4. When it comes to the treated N-Carbon sample, the intense band corresponding to C = O at 1720 cm^{-1} and the band corresponding to R – C = O at 1404 cm^{-1} and 1220 cm^{-1} faded completely.

Raman Spectroscopy was used to explore the structural defects and disorders of the produced samples in more detail. The spectra of g-C_3N_4 at different excitation wavelengths are shown in Figure 3c. As it can be seen, g-C_3N_4 did not show any peaks under 532 nm and 633 nm excitation due to its high fluorescence. However, at 780 nm and 1064 nm excitation, it exhibited the characteristic peaks attributed to g-C_3N_4 at 472 cm^{-1}, 701 cm^{-1}, 741 cm^{-1}, 980 cm^{-1} and 1236 cm^{-1} [38, 39]. When it comes to the untreated 0.5Carbon/g-C_3N_4 and treated 0.5N-Carbon/g-C_3N_4 the characteristic peaks of graphitic carbon nitride are detected (Figure 3d); however, the peaks of graphitic carbon are not detected, and this could be assigned to the low loading of carbon and to the dominance of g-C_3N_4 in the hybrid material.

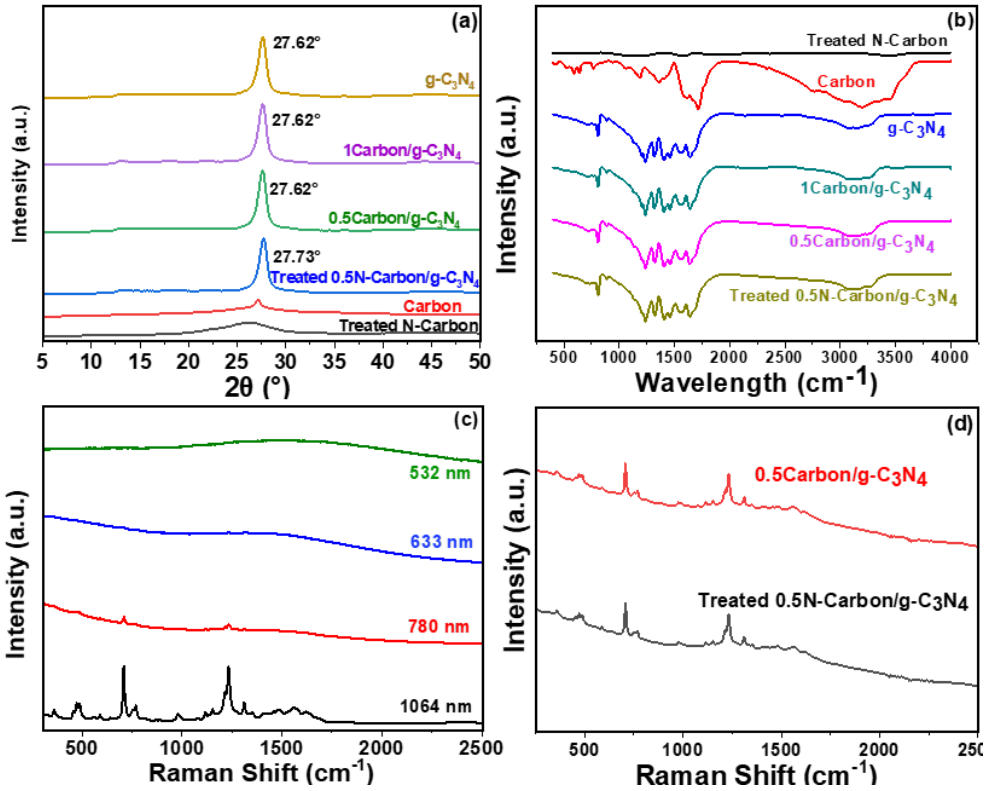

Figure 3: (a) XRD patterns of g-C_3N_4, 0.5Carbon/g-C_3N_4, treated 0.5N-Carbon/g-C_3N_4, Carbon and Treated N-Carbon, (b)FTIR spectra of treated Carbon, N-Carbon, g-C_3N_4, 0.5Carbon/g-C_3N_4, treated 0.5N-Carbon/g-C_3N_4 catalysts, (c)Raman spectra of g-C_3N_4 at different laser excitations, (d) Raman spectra of 0.5Carbon/g-C_3N_4 and treated 0.5N-Carbon/g-C_3N_4 at 1064 nm excitation.

The samples were subsequently thoroughly examined to gain more information about the observed photocatalytic performance. Figure 4 shows the wide and high-resolution C 1s, N 1s and O 1s XPS spectra in the corresponding bare g-C_3N_4, 0.5Carbon/g-C_3N_4 and treated 0.5N-Carbon/g-C_3N_4. The wide spectra showed the presence of carbon and nitrogen with similar atomic concentration in all studied materials. The content of oxygen was slightly higher in 0.5Carbon/g-C_3N_4 (2 %) compared to treated 0.5N-Carbon/g-C_3N_4 (1 %) and bare g-C_3N_4 (<1 %). The increase and decrease of O in in 0.5Carbon/g-C_3N_4 and treated 0.5N-Carbon/g-C_3N_4 composites may be related to the presence of fluorescent species with oxygen atom and their degradation after the heat treatment, respectively. After the deconvolution, the C 1s, N 1s and O 1s core-level spectra showed the same profile of functional groups in g-C_3N_4, 0.5Carbon/g-C_3N_4 and treated 0.5N-Carbon/g-C_3N_4 where the detected peaks showed a steady positions (oscillation of ±0.1 eV). The homogeneity within samples can be related to the domination of g-C_3N_4 in composite (99.5 %) [40, 41]. The C 1s spectra (Figure 4b) was composed of peaks centered at 288.1

(C1), 284.8 (C2), 286.4 (C3), 289 (C4) and 293.4 (C5) eV and attributed to sp^2 carbons of heptazine rings, C–C or C═C bonds of adventurous carbon (unintentionally incorporated into g-C_3N_4), hydroxyl groups (C–OH), carboxyl groups (COOH) and shake-up satellite, respectively. Figure 4c shows the N 1s spectra where the main peak was deconvoluted into three components with the binding energy of 398.5 (N1), 399.6 (N2), and 401.1 eV (N3) and assigned to sp^2 nitrogen on the heptazine ring (C═N– C), amino groups (C–NH_2 or C–NH–), and a central nitrogen singly bonded to three carbons N–$(C)_3$, respectively [42]. A second peak (two components at 404.1 eV and 406.2 eV) in N 1s originates from the shake-up satellite caused by charging effect. Figure 4d shows the O 1s spectra deconvoluted into two components centered at 310.7 (O1) and 533.0 (O2) eV, which are attributed to hydroxyl (C–OH) or carboxyl (COOH) groups and ether (C–O–O) groups, respectively.

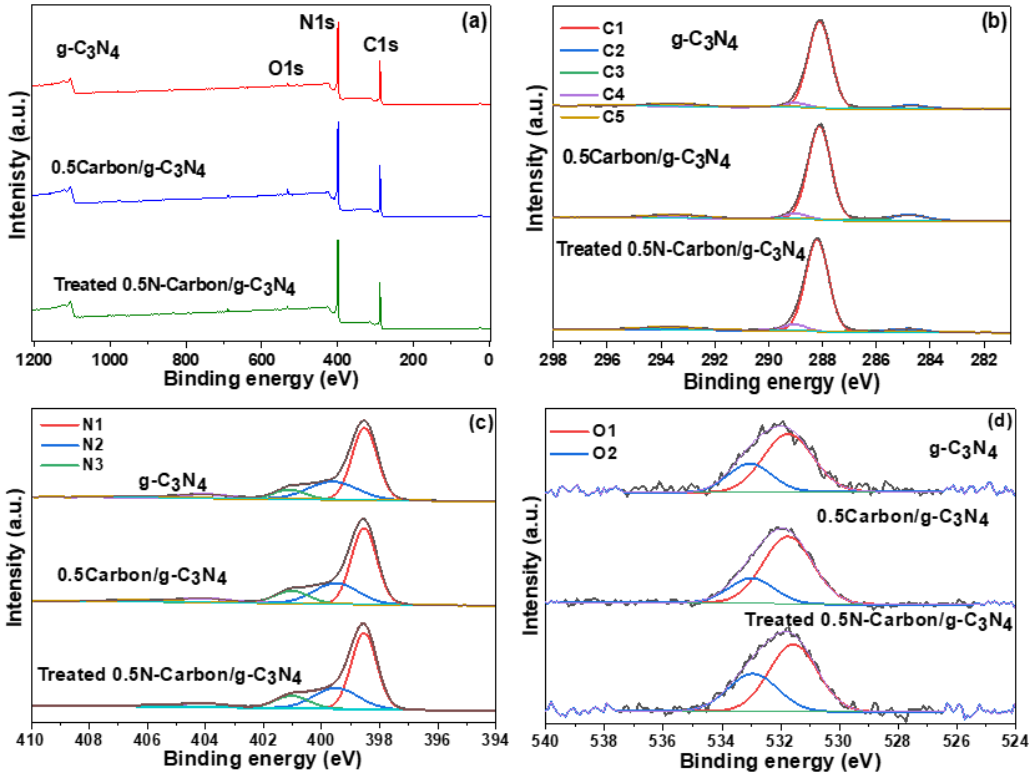

Figure 4: XPS spectra of (a) wide spectra, (b) C 1s, (c) N 1s and (d) O 1s of g-C_3N_4, 0.5Carbon/g-C_3N_4 and treated 0.5N-Carbon/g-C_3N_4. (C1: N=C–N_2, C2: C–C or C═C, C3: C–O–C, C4: COOH, C5: Shake-up satellites, N1: C═N–C, N2: C–N–H/C–NH_2, N3: N–C_3, O1: C-OH/COOH, O2: C–O).

TEM images of g-C_3N_4 and treated 0.5N-Carbon/g-C_3N_4 are shown in Figures S7a and S7b, respectively. Synthesized g-C_3N_4 showed the classic sheet-like layered structure. When it comes to the

treated 0.5N-Carbon/g-C_3N_4, although the basic morphology of the pristine g-C_3N_4 did not show any change, the detection of the N-Carbon material by TEM was not anticipated due to the low loading (0.5 wt.%). Furthermore, the inability of N-Carbon detection on catalyst's surface could also be due to the excellent dispersion of the carbon material in solution due to the oxygen and nitrogen groups on the surface or due to the integration of the N-Carbon in the core of the structure of g-C_3N_4 after the vigorous ultrasonic treatment, long mixing time, and heat treatment. This observation may be used to support the idea that a close contact between the N-Carbon and g-C_3N_4 could result in strong interfacial charge transfer and significant photocatalytic activity. Similar results were elaborated by Gu et al. where the carbon material was not detected on the surface of g-C_3N_4 [43]. A TEM image of Carbon material is present in the SI part in Figure S2.

In terms of surface area, all samples showed similar results in the range of 7 to 9 m^2/g. For more detailes, please see Table S1 in the SI part.

The absorbance profile of the studied samples is presented in Figure 5a. Compared to bare g-C_3N_4, samples doped with carbon show a wider light absorption capacity in the entire UV-visible spectrum. Incorporation of carbon materials can increase the optical absorption efficiency due to the sp^2 carbon clusters contained in the carbon layer that has a great optical absorption capacity throughout the wavelength [43]. When it comes to the band gap, the plot of hv versus α^2 gave a straight line, which means that our composite material is a direct band gap semiconductor. Similar results were found by Qu et al. [25] and Liang et al. [44]. Here, a significant shift is detected in g-C_3N_4 after N-Carbon doping and after heat treatment. The band gap increased from 2.82 eV in the case of g-C_3N_4 to 2.88 eV after 0.5Carbon doping, and reached 2.97 eV after heat treatment of the hybrid material as shown in Figure 5b. Despite the fact that the heat treated sample showed a shift in the band gap, this sample maintained visible range absorption. This change in band gap is attributed to a modification in the packing of g-C_3N_4 layers for treated N-Carbon/g-C_3N_4 sample, as revealed by the XRD analysis [28].

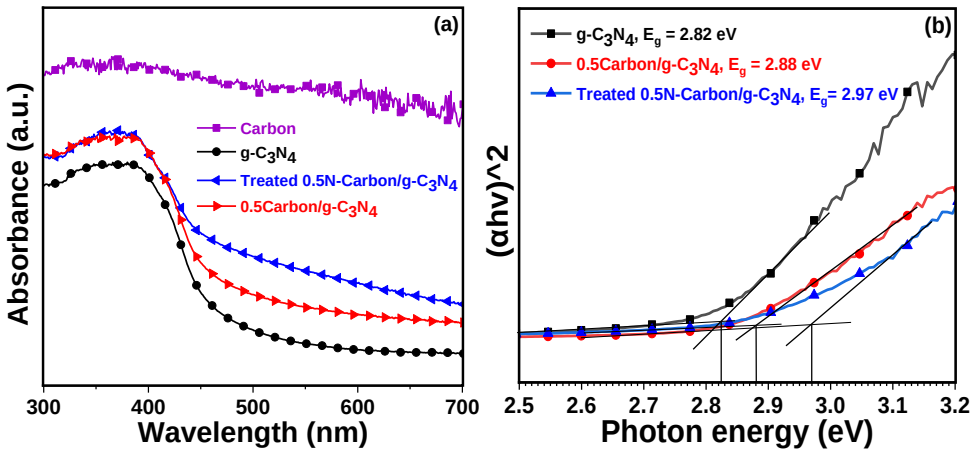

Figure 5: (a)Absorbance profile collected by UV-vis spectroscopy, (b) Tauc plot of g-C_3N_4, 0.5Carbon/g-C_3N_4 and treated 0.5N-carbon/g-C_3N_4.

Electrochemical impedance spectra (EIS) shown in Figure 6a are used to determine the charge transfer of the investigated materials. Semiconductor materials with smaller arc radius in EIS have more efficient charge carrier migration, higher conductivity, and lower electron–hole pair recombination rates [45]. Charge transfer resistance was identified as the source of the semicircle curve in the high-frequency zone in the EIS. For the three studied samples, the arc radii follow the order: Treated 1N-Carbon/g-C_3N_4 > 1Carbon/g-C_3N_4 > g-C_3N_4 > 0.5Carbon/g-C_3N_4 > Treated 0.5N-Carbon/g-C_3N_4. The small diameter of the treated 0.5N-Carbon/g-C_3N_4 indicated that this sample has the highest conductivity, the best charge transfer, and the lowest resistance. Figure 6b presents the electrostatic polarization curves of g-C_3N_4, 0.5Carbon/g-C_3N_4 and treated 0.5N-Carbon/g-C_3N_4. The latter showed the highest current density, explaining that the photoresponse capability of g-C_3N_4 and N-Carbon/g-C_3N_4 is enhanced, and more electrons are being created and transferred. Therefore, the N-Carbon material increases the photochemical properties of g-C_3N_4 after thermal treatment. The optical and electrochemical properties of the studied catalysts are summarized in Table 1.

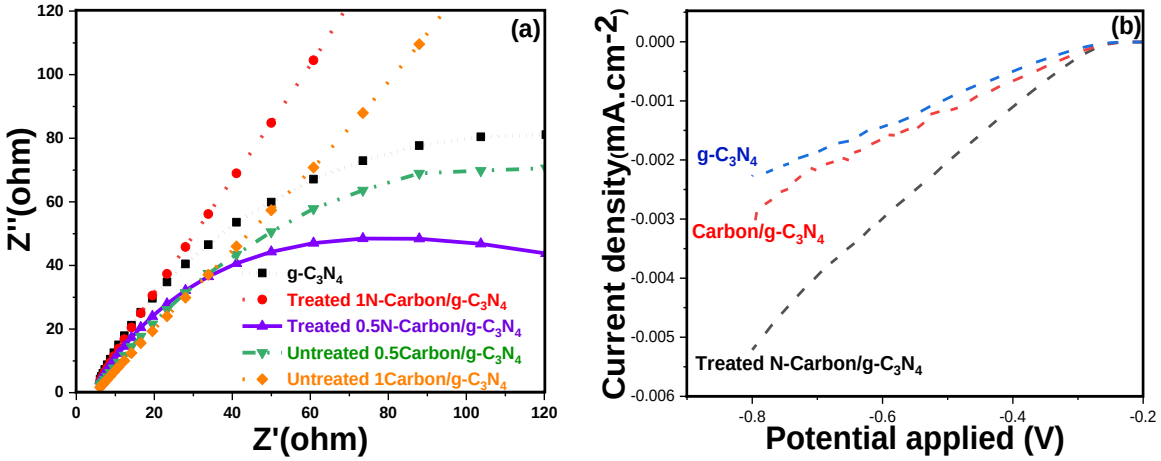

Figure 6: (a)EIS Nyquist plots g-C_3N_4, and treated N-Carbon/g-C_3N_4 and untreated Carbon/g-C_3N_4 samples, (b) Electrocatalytic polarization curves of g-C_3N_4, Carbon/g-C_3N_4 and treated N-Carbon/g-C_3N_4.

Table 1: Optical and electrochemical properties of g-C_3N_4, 0.5Carbon/g-C_3N_4 and treated 0.5N-Carbon/g-C_3N_4.

	g-C_3N_4	***0.5Carbon/g-C_3N_4***	***Treated 0.5N-Carbon/g-C_3N_4***
Band gap (eV)	2.82	2.88	2.97
Electron density ($mA.cm^{-2}$)	-0.0022	- 0.003	- 0.0053

3.2.2. Characterization of Carbon and N-Carbon

The spectroscopy characterization techniques were unable to detect the effect of carbon loading in the composite due to the domination of g-C_3N_4 (99.5 %), which was beyond the limit of the detection. Therefore, we looked independently at the structural changes of carbon before and after heat treatment that had a significant effect on electrochemical properties and photocatalytic activity in the composite.

The Raman spectra of carbon and treated N-Carbon are shown in Figure 7a. The untreated carbon sample did not show any peak, which is attributed to the presence of fluorescent species formed during its production [46, 47]. However, the heat treated N-Carbon sample showed the characteristic D (1318 cm^{-1}) and G (1580 cm^{-1}) bands of carbon-like graphitic structure corresponding to the defects or disordered sp^2 carbon atoms and to the sp^2-hybridized carbon atoms in graphitic layers, respectively

[48]. Hence, the carbon-like fluorescent species of carbon were transformed into carbon-like graphitic structure with defective sites (probably origination from N-doping) in treated N-Carbon.

The observations in Raman were further confirmed by UV-vis (Figure 7b). The UV-vis profile of carbon shows the presence of absorption bands. These bands are due to the π–π* transition of aromatic sp^2 domains (245 nm) and to the n–π* transition of C=O bonds (345 nm). Fluorescent species such as HPPT (4-hydroxy-1Hpyrrolo[3,4-c]pyridine-1,3,6(2H,5H)-trione), CTA (citrazinic acid), CYA (cyanuric acid), and citrazinic amide can contribute to the rise of the mentioned UV-vis peaks [49]. However, after heat treatment, the mentioned fluorescent species were no longer detectable. Figure 7c shows the EIS Nyquist plots of carbon and heat treated N-Carbon. The treated N-Carbon has a smaller arc radius indicating that it has a higher conductivity and more efficient charge carrier migration.

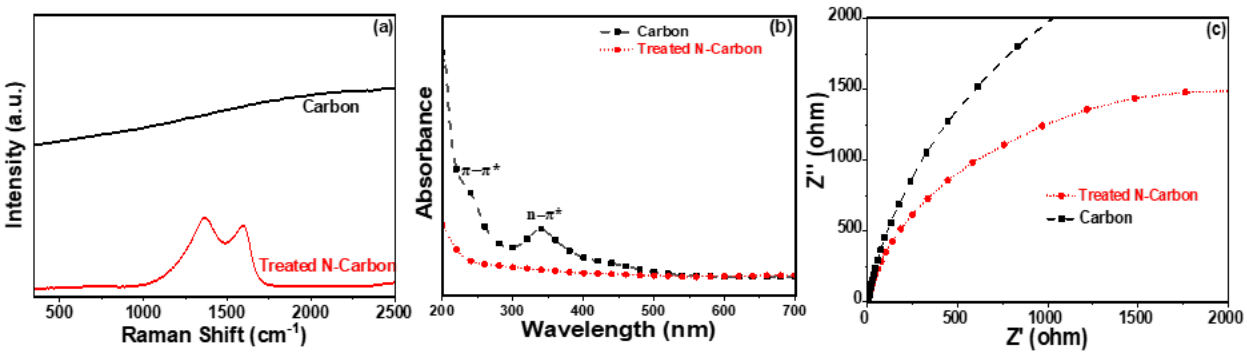

Figure 7: (a)Raman spectra of carbon and Treated N-Carbon at 532 nm excitation, (b)UV-vis carbon and treated N-Carbon (c) EIS Nyquist plots of Carbon and treated N-Carbon.

XPS analysis was used to understand how heat treatment affects the surface chemistry of carbon. The wide XPS spectra (Figure 8a) showed presence of carbon, nitrogen, and oxygen in both carbon and treated N-Carbon samples. However, the content of carbon increases while amount of oxygen decreases under heat treatment. The modification observed in XPS data of carbon and treated N-carbon suggests the degradation of carbonyl groups (loss of C4 peak in C 1s (Figure 8b) and O3 peak in O 1s (Figure 8d)) and amine groups (loss of N4 in N 1s (Figure 8c) under the heat treatment that can be related to the termination of fluorescent species (e.g. citraconic anhydride). On the other hand, the doping of N into carbon with graphitic nature was confirmed in C s and N 1s spectra of treated N-carbon. Accordingly, the characteristic peaks were detected for the C═C bonds of graphitic carbon (asymmetric C1 at 284.6

eV), Csp^2–N bonds of pyridine and pyrrolic N structures (C2 at 285.3 eV) and Csp^3–N bond of graphitic N structures (C3 at 286.4 eV) in C 1s of treated N-Carbon. The peak typical for pyridinic N (N1 at 398.4 eV), pyrrolic N mixed with tertiary amine (N2 at 400.1 eV) and graphitic N (N3 at 401.3 eV) were found in N 1s spectra of treated N-Carbon [40, 50]. The sample of treated N-Carbon showed also the presence of C−O−C groups (C3 at 286.4 eV and O2 at 535.5 eV), C−OH groups (C3 at 286.4 eV and O1 at 532.0 eV), C═O groups (C4 at 287.8 eV and O3 at 530.8 eV) and COOH groups (C5 at 289.6 eV and 532.0 eV) [51]. In summary, XPS results confirmed the domination of fluorescence species with carbonyl and amine functional groups in carbon and formation of N-doped carbon in the form of pyridine and pyrrolic structures in treated N-Carbon. The results are coherent with UV-Vis and Raman observations.

The formed N-doped Carbon with pyrrolic and pyridinic N may be connected with higher conductivity in treated N-Carbon. Similar observations were elaborated by Jiang et al. [52] and Bianco et al. [53] who reported the prominent role of pyridinic and pyrrolic nitrogen in the enhancement of electron flow in catalysts by breaking the electroneutrality of carbon networks which will favor the charge-carrier separation. These findings are in line with our electrochemical measurements where the treated N-carbon, in which pyridinic and pyrrolic functional groups emerged, showed a higher conductivity as presented in Figure 7c.

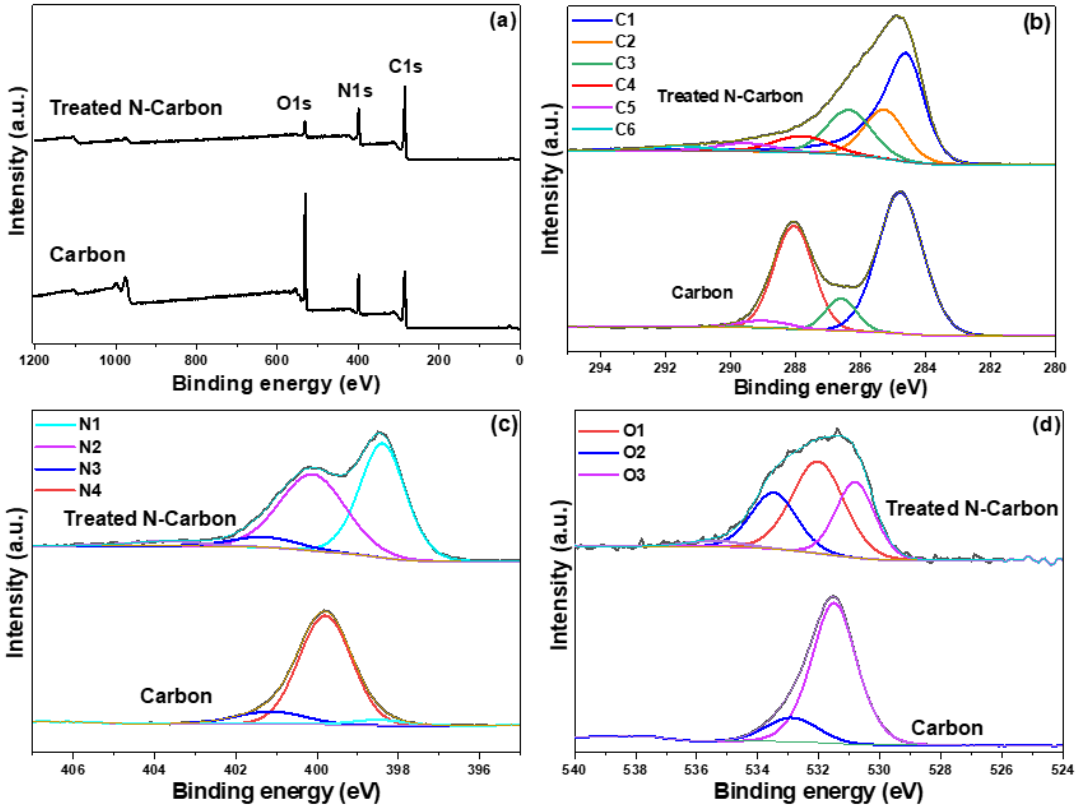

Figure 8: XPS spectra of (a) wide spectra, (b) C 1s, (c) N 1s and (d) O 1s of carbon and treated N-Carbon. (C1: C-C or C═C, C2: Csp^2–N, C3: Csp^3–N or C–O–C or C–OH, C4: C═O, C5:COOH, C6: π- π, N1: Pyridinic N, N2: Pyrrolic N or tertiary amine, N3: Graphitic N, N4: C–N–H or C– NH_2, , O1: C–OH or COOH or epoxide, O2: C–O–C, O3: C═O).*

3.3. Photocatalytic tests

3.3.1. Photocatalytic activity of g-C_3N_4

A blank degradation test is carried out under solar simulated light irradiation to determine the level of direct photolysis. Concentration of MB in the sample was measured as a function of time by UV-Vis at 665 nm. It was found that the concentration of MB in the solution under light without the presence of a catalyst decreases linearly with time (see Figure S12) with the MB degradation efficiency reaching 10% after 3 hours of irradiation.

The kinetics of MB (10 mg/L) adsorption on g-C_3N_4 at a concentration of 1 g/L was carried out in the dark to minimize any degradation. Obtained results are shown in Figure S13. As can be seen, that initially fast decay slows down at 60 min (C/C0= 0.8) and reaches plateau at 120 min (C/C0= 0.72), corresponding to a maximum adsorption capacity of 8.8 x 10^{-6} mol MB/g of g-C_3N_4.

To identify the optimal catalyst concentration, the photodegradation of MB was carried out in the presence of g-C_3N_4 catalyst at different mass concentrations, i.e., 0.5, 1 and 2 g/L, while the other reaction parameters remained the same. Figure 9a shows that the optimal concentration of catalyst for MB degradation is equal to 1 g/L. Figure S14 shows the MB adsorption and degradation kinetic. Interestingly, the degree of degradation was lower in the case of a lower or higher amount of g-C_3N_4. This can be explained in the subsequent way, where both the number of photons absorbed and the number of MB molecules adsorbed on g-C_3N_4 increase with increasing the amount of g-C_3N_4. However, over a particular threshold, the high amount of catalyst could thwart the complete illumination of the reaction medium. As a result, the additional catalyst powder does not enhance the catalytic activity, and the rate does not grow beyond a certain point as the amount of catalyst increases. A possible solution to this problem could be the employment of a thinner reaction medium so that the light can penetrate in a better way. However, in our case 1g/L mass concentration is used for further studies and a medium temperature of 22°C was maintained in all experiments.

3.3.2. Photocatalytic activity of Carbon/g-C_3N_4 and N-Carbon/g-C_3N_4

Herein, the reactions were carried out in order to determine the optimal amount of carbon doping on g-C_3N_4. The concentration of the catalyst in the medium was fixed at 1 g/L. The amounts of carbon doping on g-C_3N_4 were 0.2, 0.5 and 1 wt.%. Low loadings of carbon were also used in many studies [54-56]. In this experiment, samples were prepared by wet impregnation without any heat treatment after drying the material. All degradation reaction parameters remained the same as mentioned above. The kinetics of adsorption and degradation are presented in Figure S15. As can be seen, the ability to adsorb MB in the dark phase increases as the amount carbon loading increases. When it comes to degradation kinetics study (see Figure 9b), the sample g-C_3N_4 doped with 1wt.% of carbon showed a dramatic decrease in degradation efficiency (C/C0 = 0.57) while the 0.5Carbon/g-C_3N_4 conserved the degradation efficiency of g-C_3N_4 and finishes with a slight improvement in MB degradation (C/C0 = 0.42). When doped with a relatively high amount carbon material, the Carbon/g-C_3N_4 showed a decrease in photocatalytic activity. The reason for this decrease may be the shielding effect, where the excessive amount of carbon would obstruct some of the light absorption [57]. Pan et al. explained the

decrease of activity after carbon loading by the competition for visible light absorption and the impediment of diffusion and convection [58].

Further photocatalytic reactions were carried out to identify the effect of heat treatment on the activity of the hybrid material formed by N-Carbon and g-C_3N_4. Many publications elaborated the beneficial effect of heat treatment after doping g-C_3N_4 with carbon material [54, 59, 60]. Heat treatment did not show any advantageous effect on the 1N-Carbon/g-C_3N_4 sample (see Figure 9c). On the other hand, the treated 0.5N-Carbon/g-C_3N_4 sample showed a considerable improvement in the ability to degrade MB. The degradation efficiency after 180 min of illumination reached 90% (C/C0 = 0.1) while it was 60% (C/C0 = 0.40) in the case of untreated 0.5Carbon/g-C_3N_4 and 58% (C/C0 = 0.42) in case of bare g-C_3N_4. This is also documented by the color change of the MB solution from dark blue at the beginning of the light phase to light blue after 3 hours of treatment as shown in Figure S16. To investigate the contribution of treated N-Carbon material alone during the degradation of MB, a photocatalytic degradation experiment was conducted where only heat treated N-Carbon material was present without any amount of g-C_3N_4 in the reaction medium (Figure S17). The results of this experiment showed only a weak degradation of 10%, confirming the importance of semiconductor material for excitation and the importance of the interaction between N-Carbon material and g-C_3N_4 to enhance photocatalytic activity. This hypothesis is supported by the electrochemical measurements (Figure 6a and 6b) showing that the heat treated 0.5N-Carbon/g-C_3N_4 sample has a better electron transfer than the untreated 0.5Carbon/g-C_3N_4 sample or bare g-C_3N_4. Moreover, Figure 10 shows the photoluminescence (PL) spectra obtained with 325 nm of excitation wavelength. As it can be seen, the treated 0.5N-Carbon/g-C_3N_4 sample displayed the lowest PL intensity when compared to the bare g-C_3N_4 and to other studied samples, which explains that this composite is able to improve the separation of photo-induced carriers and to decrease the rate of recombination. To confirm the effect of N atoms on catalytic activity, a hybrid heat treated material composed of 0.5Carbon/g-C_3N_4 in which the carbon was synthesized without the presence of urea as a source of nitrogen was tested. The activity results were 20% lower than treated 0.5N-Carbon/g-C_3N_4 (Figure S18), confirming the beneficial role that nitrogen plays after heat treatment. The beneficial role of N atoms was previously explained by that pyridinic and pyrrolic N groups created after heat

treatment that enhanced the conductivity of carbon material. Moreover, the effect of heat treatment at 500°C on the bare g-C_3N_4 was tested and did not show any enhacement of activity (Figure S19).

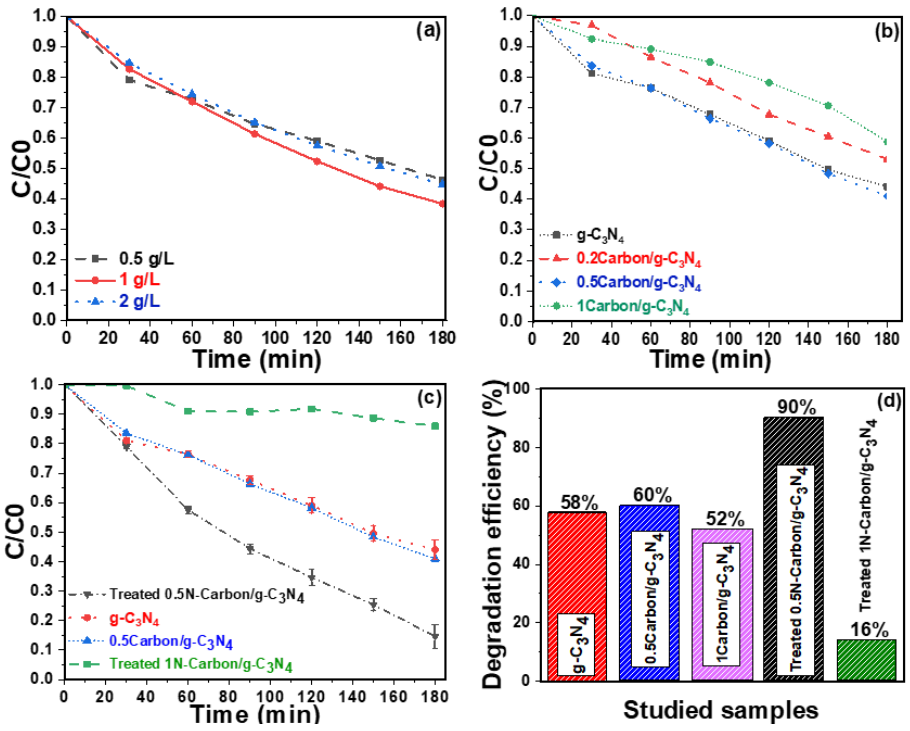

Figure 9: (a)Effect of amount of catalyst on MB degradation, (b)MB degradation for bare g-C_3N_4 and Carbon/ g-C_3N_4 composite with different loadings before heat treatment, (c)MB degradation by various treated and untreated carbon doped g-C_3N_4 samples, (d)degradation efficiency of MB over the studied catalysts under visible light irradiation.

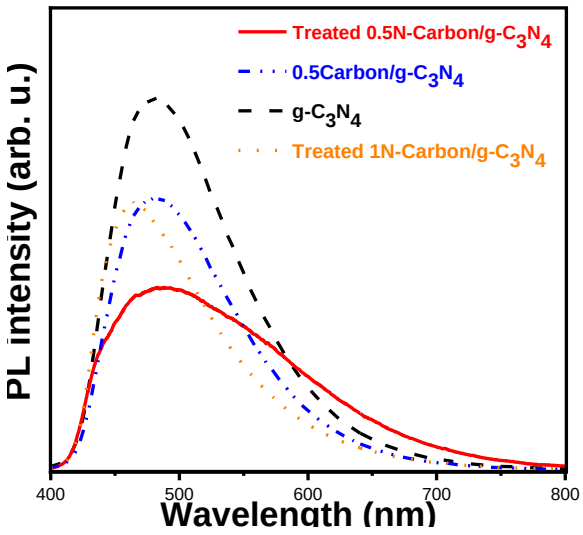

Figure 10: PL spectra of the studied photocatalysts.

3.4. Photocatalytic mechanism

Reactive species trapping experiments were conducted to understand the mechanism for MB degradation on the best active material surface. We employed IPA, Ascorbic acid and EDTA as hydroxyl (•OH), superoxide ($\bullet O_2^-$) and hole (h^+) scavengers, respectively [61, 62]. As shown in Figure S20, slight decrease in activity with EDTA implies that role of holes in MB degradation is minor, whereas other species play an important role as its inhibition results deep reduction in activity, briefly 60% and 56% less activity for hydroxyl and superoxide trapping, respectively, on the composite surface. This observation confirms that hydroxyl radicals (•OH) and superoxide ($\bullet O_2^-$) species are responsible for MB photo degradation on our material surface. In general, when a semiconductor is irradiated with light over its surface with a sufficient photon energy that exceeds its band gap energy, excited electrons move from the valence band (VB) to the conduction band (CB), creating electron/hole-pairs. CB excited electron is responsible for the reduction reactions whereas VB holes are responsible for the oxidation reactions. Furthermore, the excited electron can recombine with the holes predominantly without usage, whereas in our designed catalyst surface, the N-carbon extract electron from the CB-g-C_3N_4 (−1.03 V vs NHE [63]) thereby enhancing the life time of charge carriers as evidenced from PL spectra (Figure 10). The effectively captured electron can attack the dissolved oxygen present on the composite surface to form superoxide species (− 0.33 V vs. NHE [64]), which further react with H^+ to form hydroxyl radicals through H_2O_2 (+ 0.68 V vs. NHE [65]) formation (Eq.5.), due to its efficient conductivity nature as evidenced from EC measurements. Direct hydroxyl radicals formation from water $H_2O/\bullet OH$ (+2.4 V vs. NHE [66]) and $OH^-/^{\bullet}OH$ (1.99 V [67]) is not possible with composite surface due to lower oxidation potential of VB g-C_3N_4 (+ 1.60 V vs. NHE [68]). Competent electron trapping and conductivity characteristics nature of N-Carbon present in the composite is the crucial factor for the electron dominated reduction reactions namely superoxide and OH radical formation. Schematic representation of the MB photo degradation on the presented composite material is illustrated in the Figure 11.

$$g\text{-}C_3N_4 + hv \rightarrow e^- + h^+ \qquad (3)$$

$$e^- + O_2 \rightarrow \bullet O_2^- \qquad (4)$$

$$\bullet O_2^- + 2H^+ + e^- \rightarrow H_2O_2 \qquad (5)$$

$$H_2O_2 + e^- \rightarrow \bullet OH + OH- \qquad (6)$$

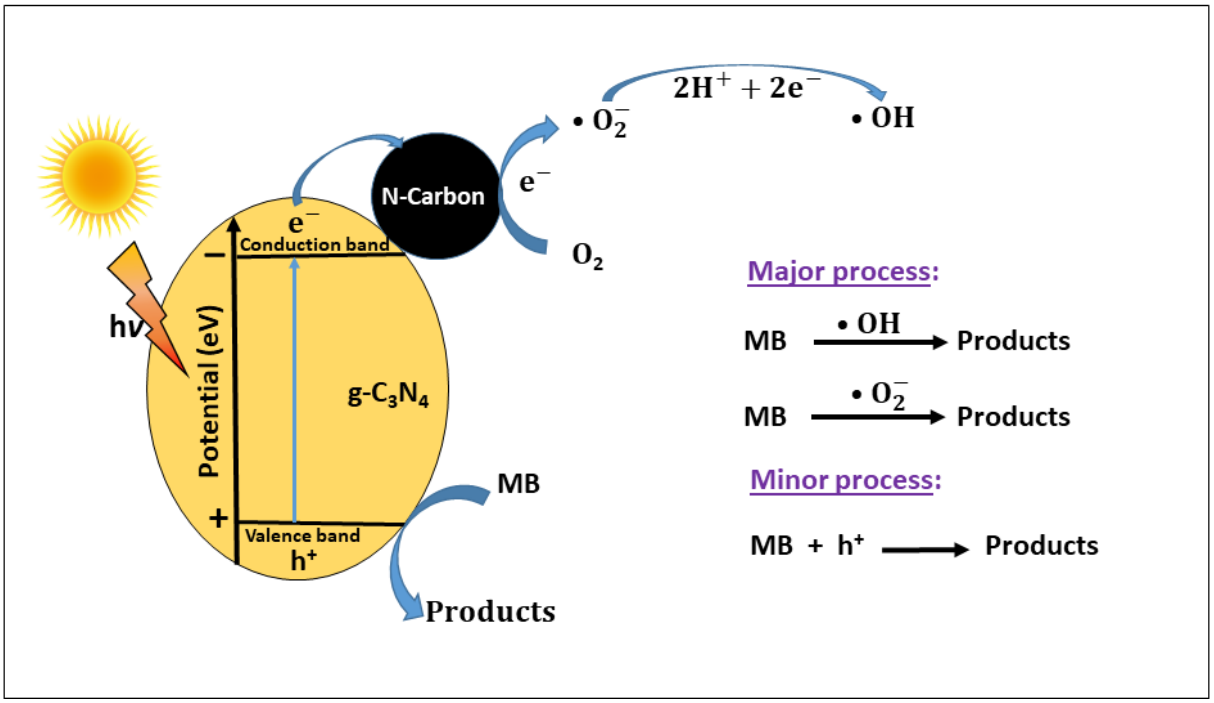

Figure 11: Photocatalytic mechanism of MB degradation by 0.5N-Carbon/g-C_3N_4.

The photocatalytic activity of N-Carbon/g-C_3N_4 was compared to the activity of other similar materials already presented in the literature. The precursor used, duration of the degradation experiment, amount of catalyst and MB concentration are important parameters to be adopted for comparison. As it can be seen in Table S2, the degradation efficiency of the bare g-C_3N_4 has been previously reported at 50% after 5h of reaction. In addition, a 90% degradation efficiency was reported when g-C_3N_4 was combined with ZnO. Therefore, our easily produced non-metallic N-Carbon/g-C_3N_4 catalyst with comparable efficiency represents an alternative to g-C_3N_4 material doped with ZnO. In addition, our studied material is a carbon-based substance and does not contain any metallic element as many hybrid materials presented in the literature.

3.5. Kinetic models analysis

The linear regression method is employed in order to obtain rate constant of the process. Considering the pseudo-first order kinetic with respect to MB concentration, there exists an analytical solution of the equation in the form (Eq.2):

$$\ln \frac{C_0}{C} = kt, \qquad (2)$$

where k is the rate constant (min^{-1}), t is the reaction time (min), C_0 is the starting concentration of MB in solution (10 mg/L), C is the concentration of MB at time t.

As shown in Table 2 and in Figure S21, a high regression coefficient R^2 confirmed validity of pseudo-first order kinetics, which is in a good agreement with literature for MB degradation [69, 70]. These results are parallel to those of the activity measurements in which hybridized compounds showed a decrease in activity. Furthermore, these results can be associated to the electrochemical measurements, in which only the treated 0.5N-Carbon/g-C_3N_4 sample showed an enhancement in conductivity. However, the increase in carbon loading led to a decrease in activity and this could be linked to the shielding effect fulfilled by the carbon material on g-C_3N_4 as explained before. On the other hand, the computed reaction rates were also in accordance with the finding, where the treated 0.5N-Carbon/g-C_3N_4 sample manifested the highest reaction rate (0.0102 min^{-1}) followed by 0.5Carbon/g-C_3N_4 (0.0066 min^{-1}) and the pristine g-C_3N_4 (0.0044 min^{-1}) respectively.

Table 2: Pseudo-first order kinetics results of MB photodegradation by various studied g-C_3N_4 catalysts.

	***k* (min^{-1})**	***R^2***
g-C_3N_4	0.0044	0.989
1Carbon/ g-C_3N_4	0.0027	0.932
0.5Carbon/ g-C_3N_4	0.0066	0.9645
0.2Carbon/ g-C_3N_4	0.0037	0.9843
Treated 0.5N-Carbon/g-C_3N_4	**0.0102**	**0.9827**
Treated 1N-Carbon/g-C_3N_4	0.001	0.9719

3.6. Stability analysis:

3.6.1. Thermal stability:

The thermogravimetric (TG) analysis was used to assess the thermodynamic stability of as-prepared samples in an air atmosphere (Figure S22). The tested material showed a great thermal stability till 570°C. However, a dramatic loss is observed in the range of 570 to 620°C, which can be attributed to the loss in tris-triazine-based units of g-C_3N_4. The good thermal stability makes this material a potential candidate for other application where a high temperature condition could be required.

3.6.2. Photocatalytic stability:

The photocatalytic degradation of MB under visible-light irradiation was repeated 4 times to test the photochemical stability of treated 0.5N-Carbon/g-C_3N_4 photocatalysts. Even after 4 consecutive experimental runs, the treated 0.5N-Carbon/g-C_3N_4 photocatalyst still degrades MB effectively, as shown in Figure 12a. In addition, the nearly unchanged XRD pattern of the reused treated 0.5N-Carbon/g-C_3N_4 (Figure 12b) indicated phase and structure stability. As a result, the treated 0.5N-Carbon/g-C_3N_4 catalyst degrades MB with high stability under visible-light irradiation and can be used as high performance visible-light photocatalysts for pollutant removal in the environment.

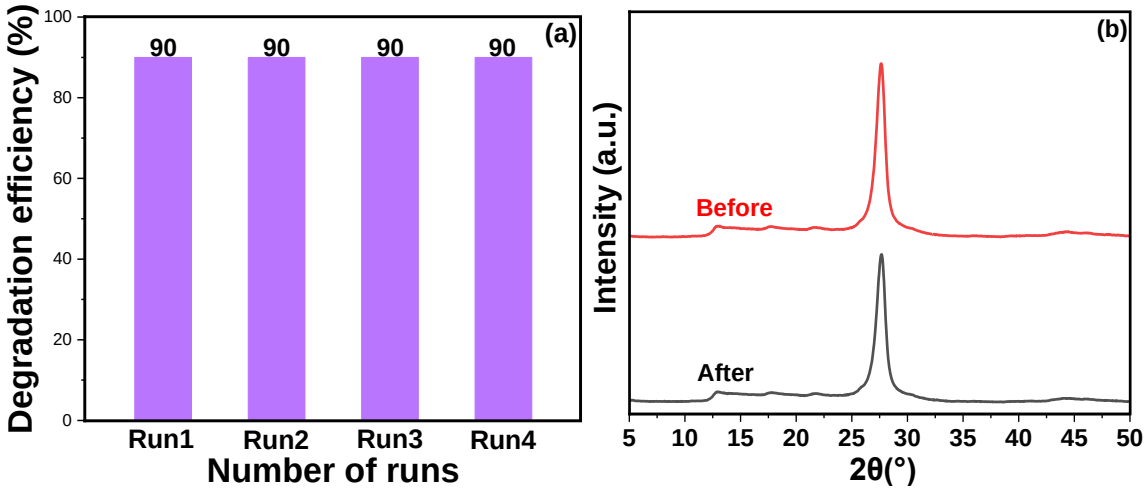

Figure 12: (a)Reusability study results, (b)XRD patterns of treated 0.5N-Carbon/g-C_3N_4 before and after usage.

4. Conclusions

In this study, it has been shown that g-C_3N_4 hybridized with N-Carbon material through wet impregnation followed by heat treatment is an effective and stable photocatalyst for the degradation of MB under simulated solar light. The results exhibited the highest photocatalytic activity for a heat treated 0.5 wt.% N-Carbon loading on g-C_3N_4 combined with a concentration of catalyst of 1 g/L. Under these conditions MB degradation efficiency of 90% at 180 minutes is attained. The comparison between heat treated 0.5N-Carbon/g-C_3N_4 and non-treated 0.5Carbon/g-C_3N_4 samples revealed the importance of heat

treatment on the photocatalytic activity of this hybrid material. This result was explained by the formation of carbon-like graphitic structure doped with pyridinic and pyrrolic nitrogen groups under heat treatment, while the carbon material contained fluorescent species before treatment. We believe that the emergence of pyrrolic and pyridinic nitrogen groups in N-Carbon is behind the enhancement of electron transfer in treated 0.5 wt.% N-Carbon/g-C_3N_4. The absence of MB degradation when treated N-Carbon is employed alone (without g-C_3N_4), confirmed that boosting of the electrochemical properties of g-C_3N_4 is due to the interaction between the latter and treated N-Carbon material and not the treated N-Carbon alone. Therefore, based on the findings of this research, it is suggested that the reasons behind the enhancement of the photocatalytic activity of g-C_3N_4 by treated N-Carbon was clarified and this work opens the door for additional research into the production of affordable, and environmentally friendly semiconductors for use in modern technology.

Acknowledgements

The authors gratefully acknowledge the support from the Technology Agency of the Czech Republic & the Research Council of Norway through the project METAMORPH (EEA & Norway Grant project TO01000329) and the specific university grants (A1_FCHI_2022_006) and (A2_FCHI_2022_020) and "The Grant Agency of the Czech Republic" (GAČR 20-21105Y) for their support.

Declaration of interests

The authors declare that they have no known competing financial interests or personal relationships that could have appeared to influence the work reported in this paper.

References

1. Hoque, M.A. and M.I. Guzman, *Photocatalytic activity: experimental features to report in heterogeneous photocatalysis.* Materials, 2018. **11**(10): p. 1990. DOI: 10.3390/ma11101990
2. Koe, W.S., et al., *An overview of photocatalytic degradation: photocatalysts, mechanisms, and development of photocatalytic membrane.* Environmental Science and Pollution Research, 2020. **27**(3): p. 2522-2565. DOI: 10.1007/s11356-019-07193-5
3. Rafiq, A., et al., *Photocatalytic degradation of dyes using semiconductor photocatalysts to clean industrial water pollution.* Journal of Industrial and Engineering Chemistry, 2021. **97**: p. 111-128. DOI: 10.1016/j.jiec.2021.02.017
4. D'amato, C., et al., *Enhancement of visible-light photoactivity by polypropylene coated plasmonic Au/TiO2 for dye degradation in water solution.* Applied Surface Science, 2018. **441**: p. 575-587. DOI: 10.1016/j.apsusc.2018.01.290
5. Desalegn, B.Z., H.S. Jadhav, and J.G. Seo, *Highly Efficient g-C3N4 Nanorods with Dual Active Sites as an Electrocatalyst for the Oxygen Evolution Reaction.* ChemCatChem, 2019. **11**(12): p. 2870-2878. DOI: 10.1002/cctc.201900330
6. Huang, D., et al., *Megamerger in photocatalytic field: 2D g-C3N4 nanosheets serve as support of 0D nanomaterials for improving photocatalytic performance.* Applied Catalysis B: Environmental, 2019. **240**: p. 153-173. DOI: 10.1016/j.apcatb.2018.08.071
7. Yang, L., et al., *Accelerated photocatalytic oxidation of carbamazepine by a novel 3D hierarchical protonated g-C3N4/BiOBr heterojunction: performance and mechanism.* Applied Surface Science, 2019. **473**: p. 527-539. DOI: 10.1016/j.apsusc.2018.12.180
8. Fu, J., et al., *Hierarchical porous O-doped g-C3N4 with enhanced photocatalytic CO2 reduction activity.* Small, 2017. **13**(15): p. 1603938. DOI: 10.1002/smll.201603938
9. Kadam, A.N., H. Kim, and S.-W. Lee, *Low-temperature in situ fabrication of porous S-doped g-C3N4 nanosheets using gaseous-bubble template for enhanced visible-light photocatalysis.* Ceramics International, 2020. **46**(18): p. 28481-28489. DOI: 10.1016/j.ceramint.2020.08.005
10. Wang, Y., et al., *Effect of nonmetal element dopants on photo-and electro-chemistry performance of ultrathin g-C3N4 nanosheets.* International Journal of Hydrogen Energy, 2020. **45**(33): p. 16519-16527. DOI: 10.1016/j.ijhydene.2020.04.110
11. Yang, L., et al., *Enhanced photocatalytic activity of g-C3N4 2D nanosheets through thermal exfoliation using dicyandiamide as precursor.* Ceramics International, 2018. **44**(17): p. 20613-20619. DOI: 10.1016/j.ceramint.2018.06.105
12. He, B., et al., *One-pot construction of chitin-derived carbon/g-C3N4 heterojunction for the improvement of visible-light photocatalysis.* Applied Surface Science, 2020. **527**: p. 146737. DOI: 10.1016/j.apsusc.2020.146737
13. Elsayed, M.H., et al., *Visible-light-driven hydrogen evolution using nitrogen-doped carbon quantum dot-implanted polymer dots as metal-free photocatalysts.* Applied Catalysis B: Environmental, 2021. **283**: p. 119659. DOI: 10.1016/j.apcatb.2020.119659
14. Gong, K., et al., *Nitrogen-doped carbon nanotube arrays with high electrocatalytic activity for oxygen reduction.* science, 2009. **323**(5915): p. 760-764. DOI: 10.1126/science.1168049
15. Li, K., F.-Y. Su, and W.-D. Zhang, *Modification of g-C3N4 nanosheets by carbon quantum dots for highly efficient photocatalytic generation of hydrogen.* Applied Surface Science, 2016. **375**: p. 110-117. DOI: 10.1016/j.apsusc.2016.03.025
16. Xu, Q., et al., *Making co-condensed amorphous carbon/g-C3N4 composites with improved visible-light photocatalytic H2-production performance using Pt as cocatalyst.* Carbon, 2017. **118**: p. 241-249. DOI: 10.1016/j.carbon.2017.03.052
17. Zhou, Y., et al., *N-doped graphitic carbon-incorporated g-C3N4 for remarkably enhanced photocatalytic H2 evolution under visible light.* Carbon, 2016. **99**: p. 111-117. DOI: 10.1016/j.carbon.2015.12.008

18. Yang, X.-C., et al., *Facile synthesis of porous nitrogen doped carbon dots (NCDs)@ g-C3N4 for highly efficient photocatalytic and anti-counterfeiting applications.* Applied Surface Science, 2019. **490**: p. 592-597. DOI: 10.1016/j.apsusc.2019.05.367
19. Wang, C., et al., *Facile synthesis of nanoporpous graphitic carbon nitride photocatalyst coupled with N-doped graphene quantum dots for efficient photo-degradation dyes under nature solar light radiation.* Diamond and Related Materials, 2018. **89**: p. 197-205. DOI: 10.1016/j.diamond.2018.09.012
20. Wang, J., et al., *Two-dimensional graphitic carbon nitride/N-doped carbon with a direct Z-scheme heterojunction for photocatalytic generation of hydrogen.* Nanoscale Advances, 2021. **3**(23): p. 6580-6586. DOI: 10.1039/D1NA00629K
21. Seng, R.X., et al., *Nitrogen-doped carbon quantum dots-decorated 2D graphitic carbon nitride as a promising photocatalyst for environmental remediation: a study on the importance of hybridization approach.* Journal of environmental management, 2020. **255**: p. 109936. DOI: 10.1016/j.jenvman.2019.109936
22. Ng, H.M., G. Lim, and C. Leo, *Comparison between hydrothermal and microwave-assisted synthesis of carbon dots from biowaste and chemical for heavy metal detection: A review.* Microchemical Journal, 2021. **165**: p. 106116. DOI: 10.1016/j.microc.2021.106116
23. Gao, T., et al., *Printed solid state electrolyte carbon nanotube thin film transistors for sub-1 V fully printed flexible CMOS inverters.* Journal of Materials Chemistry C, 2021. **9**(21): p. 6852-6862. DOI: 10.1039/D1TC00357G
24. Vercelli, B., *The role of carbon quantum dots in organic photovoltaics: a short overview.* Coatings, 2021. **11**(2): p. 232. DOI: 10.3390/coatings11020232
25. Qu, D., et al., *Peering into water splitting mechanism of g-C3N4-carbon dots metal-free photocatalyst.* Applied Catalysis B: Environmental, 2018. **227**: p. 418-424. DOI: 10.1016/j.apcatb.2018.01.030
26. Yuan, Y.-P., et al., *Red phosphor/g-C3N4 heterojunction with enhanced photocatalytic activities for solar fuels production.* Applied Catalysis B: Environmental, 2013. **140**: p. 164-168. DOI: 10.1016/j.apcatb.2013.04.006
27. Xu, J., et al., *Mg-induced g-C3N4 synthesis of nitrogen-doped graphitic carbon for effective activation of peroxymonosulfate to degrade organic contaminants.* Chinese Chemical Letters, 2021. DOI: 10.1016/j.cclet.2021.10.005
28. Papailias, I., et al., *Novel torus shaped g-C3N4 photocatalysts.* Applied Catalysis B-environmental, 2020. **268**: p. 118733.
29. Mishra, A., et al., *Graphitic carbon nitride (g–C3N4)–based metal-free photocatalysts for water splitting: a review.* Carbon, 2019. **149**: p. 693-721. DOI: 10.1016/j.carbon.2019.04.104
30. Raikwar, V., *Synthesis and study of carbon quantum dots (CQDs) for enhancement of luminescence intensity of CQD@ LaPO4: Eu3+ nanocomposite.* Materials Chemistry and Physics, 2022. **275**: p. 125277. DOI: 10.1016/j.matchemphys.2021.125277
31. Yan, S., Z. Li, and Z. Zou, *Photodegradation performance of g-C3N4 fabricated by directly heating melamine.* Langmuir, 2009. **25**(17): p. 10397-10401. DOI: 10.1021/la900923z
32. Li, X., et al., *Preparation and characterization of graphitic carbon nitride through pyrolysis of melamine.* Applied Physics A, 2009. **94**(2): p. 387-392. DOI: 10.1007/s00339-008-4816-4
33. Yang, Z., et al., *BiOBr/protonated graphitic C3N4 heterojunctions: intimate interfaces by electrostatic interaction and enhanced photocatalytic activity.* Journal of Alloys and Compounds, 2015. **634**: p. 215-222. DOI: 10.1016/j.jallcom.2015.02.103
34. Dong, F., et al., *Facile transformation of low cost thiourea into nitrogen-rich graphitic carbon nitride nanocatalyst with high visible light photocatalytic performance.* Catalysis Science & Technology, 2012. **2**(7): p. 1332-1335. DOI: 10.1039/C2CY20049J
35. Yang, X., et al., *Facile fabrication of acidified g-C3N4/g-C3N4 hybrids with enhanced photocatalysis performance under visible light irradiation.* Applied Catalysis B: Environmental, 2016. **193**: p. 22-35. DOI: 10.1016/j.apcatb.2016.03.060

36. Bojdys, M.J., et al., *Ionothermal synthesis of crystalline, condensed, graphitic carbon nitride.* Chemistry–A European Journal, 2008. **14**(27): p. 8177-8182. DOI: 10.1002/chem.200800190
37. Hinterberger, V., et al., *Purification and structural elucidation of carbon dots by column chromatography.* Nanoscale, 2019. **11**(17): p. 8464-8474. DOI: 10.1039/C9NR01029G
38. Jing, Y., et al., *High-yield production of g-C3N4 quantum dots as photocatalysts for the degradation of organic pollutants and fluorescent probes for detection of Fe3+ ions with live cell application.* Applied Surface Science, 2022. **586**: p. 152812. DOI: 10.1016/j.apsusc.2022.152812
39. Papailias, I., et al., *Effect of processing temperature on structure and photocatalytic properties of g-C3N4.* Applied Surface Science, 2015. **358**: p. 278-286. DOI: 10.1016/j.apsusc.2015.08.097
40. Ayiania, M., et al., *Deconvoluting the XPS spectra for nitrogen-doped chars: An analysis from first principles.* Carbon, 2020. **162**: p. 528-544. DOI: 10.1016/j.carbon.2020.02.065
41. Jana, B., et al., *Carbon nanodots for all-in-one photocatalytic hydrogen generation.* Journal of the American Chemical Society, 2021. **143**(48): p. 20122-20132. DOI: 10.1021/jacs.1c07049
42. Akaike, K., et al., *Characterizing electronic structure near the energy gap of graphitic carbon nitride based on rational interpretation of chemical analysis.* Chemistry of Materials, 2018. **30**(7): p. 2341-2352. DOI: 10.1021/acs.chemmater.7b05316
43. Gu, J., et al., *Fe3O4-loaded g-C3N4/C-layered composite as a ternary photocatalyst for tetracycline degradation.* ACS omega, 2020. **5**(48): p. 30980-30988. DOI: 10.1021/acsomega.0c03905
44. Liang, J., et al., *Integrating optimal amount of carbon dots in g-C3N4 for enhanced visible light photocatalytic H2 evolution.* International Journal of Hydrogen Energy, 2022. **47**(41): p. 18032-18043. DOI: 10.1016/j.ijhydene.2022.03.285
45. Hong, S.J., et al., *Heterojunction BiVO4/WO3 electrodes for enhanced photoactivity of water oxidation.* Energy and Environmental Science, 2011. **4**: p. 1781-1787. DOI: 10.1039/C0EE00743A
46. Luo, P., C. Li, and G. Shi, *Synthesis of gold@ carbon dots composite nanoparticles for surface enhanced Raman scattering.* Physical Chemistry Chemical Physics, 2012. **14**(20): p. 7360-7366. DOI: 10.1039/C2CP40767A
47. Yang, Z., et al., *Nitrogen-doped, carbon-rich, highly photoluminescent carbon dots from ammonium citrate.* Nanoscale, 2014. **6**(3): p. 1890-1895. DOI: 10.1039/C3NR05380F
48. Wang, D., et al., *Coal tar pitch derived N-doped porous carbon nanosheets by the in-situ formed g-C3N4 as a template for supercapacitor electrodes.* Electrochimica Acta, 2018. **283**: p. 132-140. DOI: 10.1016/j.electacta.2018.06.151
49. Vallan, L. and H. Imahori, *Citric acid-based carbon dots and their application in energy conversion.* ACS Applied Electronic Materials, 2022. **4**(9): p. 4231-4257. DOI: 10.1021/acsaelm.2c01021
50. Smith, M., et al., *Improving the deconvolution and interpretation of XPS spectra from chars by ab initio calculations.* Carbon, 2016. **110**: p. 155-171. DOI: 10.1016/j.carbon.2016.09.012
51. Ludmerczki, R., et al., *Carbon dots from citric acid and its intermediates formed by thermal decomposition.* Chemistry–A European Journal, 2019. **25**(51): p. 11963-11974. DOI: Carbon dots from citric acid and its intermediates formed by thermal decomposition
52. Jiang, H., et al., *Effect of pyridinic-and pyrrolic-nitrogen on electrochemical performance of Pd for formic acid electrooxidation.* Electrochimica Acta, 2020. **337**: p. 135758. DOI: 10.1016/j.electacta.2020.135758
53. Bianco, G.V., et al., *Effective hole conductivity in nitrogen-doped CVD-graphene by singlet oxygen treatment under photoactivation conditions.* Scientific Reports, 2022. **12**(1): p. 1-11. DOI: 10.1038/s41598-022-12696-2

54. Xu, S., et al., *Introduction of porous structure via facile carbon-dot modulation: A feasible and promising approach for improving the photocatalytic capability of sulfur doped g-C3N4.* Catalysis Today, 2019. DOI: 10.1016/j.cattod.2019.02.017
55. Wang, F., et al., *Facile synthesis of N-doped carbon dots/g-C3N4 photocatalyst with enhanced visible-light photocatalytic activity for the degradation of indomethacin.* Applied Catalysis B-environmental, 2017. **207**: p. 103-113. DOI: 10.1016/j.apcatb.2017.02.024
56. Shi, W.l., et al., *Carbon dots anchored high-crystalline g-C3N4 as a metal-free composite photocatalyst for boosted photocatalytic degradation of tetracycline under visible light.* Journal of Materials Science, 2020. **56**: p. 2226 - 2240. DOI: 10.1007/s10853-020-05436-2
57. Jiao, Y., et al., *A novel MoS2 quantum dots (QDs) decorated Z-scheme g-C3N4 nanosheet/N-doped carbon dots heterostructure photocatalyst for photocatalytic hydrogen evolution.* Applied Catalysis B: Environmental, 2019. DOI: 10.1016/j.apcatb.2019.01.073
58. Pan, J., et al., *Preparation of carbon quantum dots/TiO 2 nanotubes composites and their visible light catalytic applications.* Journal of Materials Chemistry A, 2014. **2**(42): p. 18082-18086. DOI: 10.1039/C4TA03528C
59. Asadzadeh-Khaneghah, S., A. Habibi-Yangjeh, and S. Vadivel, *Fabrication of novel g-C3N4 nanosheet/carbon dots/Ag6Si2O7 nanocomposites with high stability and enhanced visible-light photocatalytic activity.* Journal of the Taiwan Institute of Chemical Engineers, 2019. DOI: 10.1016/j.jtice.2019.07.018
60. Jiao, Y., et al., *Exfoliation-induced exposure of active sites for g-C3N4/N-doped carbon dots heterojunction to improve hydrogen evolution activity.* Molecular Catalysis, 2020. **497**: p. 111223. DOI: 10.1016/j.mcat.2020.111223
61. Xin, G. and Y. Meng, *Pyrolysis synthesized g-C3N4 for photocatalytic degradation of methylene blue.* Journal of Chemistry, 2013. **2013**. DOI: 10.1155/2013/187912
62. Bai, X., et al., *Enhanced oxidation ability of g-C3N4 photocatalyst via C60 modification.* Applied Catalysis B: Environmental, 2014. **152**: p. 262-270. DOI: 10.1016/j.apcatb.2014.01.046
63. Ma, X., et al., *A strategy of enhancing the photoactivity of g-C3N4 via doping of nonmetal elements: a first-principles study.* The Journal of Physical Chemistry C, 2012. **116**(44): p. 23485-23493.
64. Ding, X., et al., *Self doping promoted photocatalytic removal of no under visible light with bi2moo6: Indispensable role of superoxide ions.* Applied Catalysis B: Environmental, 2016. **182**: p. 316-325.
65. Wang, Y.-H., B. Mondal, and S.S. Stahl, *Molecular Cobalt Catalysts for O2 Reduction to H2O2: Benchmarking catalyst performance via rate–overpotential correlations.* ACS Catalysis, 2020. **10**(20): p. 12031-12039.
66. Jiang, C., et al., *Photoelectrochemical devices for solar water splitting–materials and challenges.* Chemical Society Reviews, 2017. **46**(15): p. 4645-4660.
67. Zhao, Z., et al., *Mass-controlled direct synthesis of graphene-like carbon nitride nanosheets with exceptional high visible light activity. Less is better.* Scientific reports, 2015. **5**(1): p. 1-15.
68. Liu, J., *Effect of phosphorus doping on electronic structure and photocatalytic performance of g-C3N4: insights from hybrid density functional calculation.* Journal of Alloys and Compounds, 2016. **672**: p. 271-276.
69. Houas, A., et al., *Photocatalytic degradation pathway of methylene blue in water.* Applied Catalysis B-environmental, 2001. **31**: p. 145-157. DOI: 10.1016/S0926-3373(00)00276-9
70. Deshmukh, S.P., et al., *Ultrasound assisted preparation of rGO/TiO2 nanocomposite for effective photocatalytic degradation of methylene blue under sunlight.* Nano-Structures and Nano-Objects, 2020. **21**: p. 100407. DOI: 10.1016/j.nanoso.2019.100407